PERGAMON

International Journal of Solids and Structures 37 (2000) 4061–4082

INTERNATIONAL JOURNAL OF SOLIDS and STRUCTURES

www.elsevier.com/locate/ijsolstr

# A localization capturing FE-interface based on regularized strong discontinuities at large inelastic strains

Paul Steinmann*, Peter Betsch

*Chair for Applied Mechanics, Department of Mechanical Engineering, University of Kaiserslautern, P.O. Box 3049, D-67653, Kaiserslautern, Germany*

Received 18 September 1998; in revised form 11 December 1998

**Abstract**

The objective of this work is the development of a finite element interface formulation tailored to capture localization within geometrically nonlinear solid mechanics. In this context, strong discontinuities are considered as the final failure mechanism within localization problems. The failure kinematics are governed by a jump in the nonlinear deformation map across a discontinuity surface. In the finite element discretization the interface element is endowed with these kinematics. As a consequence, the interface stiffness is dominated by the weighted spatial localization tensor. Based on these developments a localization capturing procedure is advocated and is computationally highlighted. 

*Keywords:* Localization; Strong discontinuities; Large inelastic strain; FE-technology

## 1. Introduction

The intensive accumulation of large inelastic deformations within narrow bands with finite width is a failure mechanism termed localization. Localization is a frequently encountered failure phenomenon in different materials and is considered as a precursor to discrete fracture. If the typical length scale of the localization zone is small compared to the characteristic dimensions of the solution domain under consideration, localized failure may be described as the development of a strong discontinuity.

The kinematical concept of strong discontinuities has been proposed for the computational description of localization bands in terms of an interface discretization by Larsson et al. (1993) and was later on adopted by Miehe and Schröder (1994). Along the same lines, e.g. Simo et al. (1993), Larsson

* Corresponding author. Web page: http://mechanik.mv.uni-kl.de/ Tel.: +49-0631-205-2419; fax: +49-0631-250-2128.
*E-mail address:* ps@rhrk.uni-kl.de (P. Steinmann).

0020-7683/00/$ - see front matter 
PII: S0020-7683(99)00141-9

and Runesson (1996) and Oliver (1996) directly embedded strong discontinuities into the domain of a finite element based on the enhanced strain concept. These alternative strategies were also applied to geometrically linear fluid saturated porous media by Larsson et al. (1996) and Steinmann (1999). Extensions of the strong discontinuity concept to large strain multiplicative elasto-plasticity were advocated by Armero and Garikipati (1996) and Steinmann et al. (1997) from where we borrow terminology and notation.

It is the aim of this contribution to incorporate regularized strong discontinuities as a kinematic model for localization bands within the geometrically nonlinear description of an inelastic solid. To this end we follow the strategy of incorporating interface elements along element edges which have to be aligned with the possible localization band in advance. Thereby, the central question is how to design the interface constitutive behaviour?

It is obvious that we basically have to set up a relation between the spatial traction vector acting on the interface and the relative deformation of the two interface sides, whereby certainly, alternative selections are possible. Different, basically geometrically linear, interface discretizations for various purposes have been proposed and analysed, see e.g. Gens et al. (1988) and Schellekens and de Borst (1993) and references therein. Here, for its conceptional beauty and simplicity, we shall extend the geometrically linear proposal by Larsson et al. (1993) which is based on a kinematic assumption for the interface strains and which results essentially in a projection of the constitutive behaviour in the continuous ambient domain onto the discontinuity. Thus, the construction of a separate interface constitutive law for the traction vector is circumvented.

The manuscript is organized as follows: first, the set-up of the boundary value problem of a geometrically nonlinear solid is reviewed in strong form. Then strong discontinuities at large strains together with their regularized counterparts are characterized kinematically. Based on the strong form of the BVP the corresponding weak form is established. To this end, we consider firstly, continuity of the deformation map and secondly, the additional contribution to the virtual work expression which is due to a discontinuous deformation map. In the sequel we are concerned with the formulation of the interface constitutive law based on the kinematic structure of a regularized strong discontinuity. Next, aspects of the linearization and the discretization into a finite element formulation are discussed. Finally, after emphasizing a three step localization capturing procedure, conceptional examples demonstrate the quantitative and qualitative performance of the advocated strategy for localization problems at large strains.

## 2. Strong form of a geometrically nonlinear BVP

To set the stage we briefly reiterate the boundary value problem of geometrically nonlinear continuum mechanics in strong form.

Let $\mathscr{B} \subset \mathbb{R}^{n_{\text{dim}}}$ denote the current configuration occupied by a solid with reference placements in $\mathscr{B}_0 \subset \mathbb{R}^{n_{\text{dim}}}$ denoted by $\boldsymbol{X}$. The boundary $\partial\mathscr{B}$ of $\mathscr{B}$ with outward normal $\boldsymbol{n}$ is subdivided into disjoint parts $\partial\mathscr{B} = \partial\mathscr{B}_x \cup \partial\mathscr{B}_t$ with $\partial\mathscr{B}_x \cap \partial\mathscr{B}_t = \emptyset$ where either Neumann or Dirichlet boundary conditions are prescribed. The current placements of the solid are described by the nonlinear deformation map $\boldsymbol{\varphi}: \mathscr{B}_0 \rightarrow \mathscr{B}$ with $\boldsymbol{x} = \boldsymbol{\varphi}(\boldsymbol{X})$. The current density is denoted by $\rho: \mathscr{B} \rightarrow \mathbb{R}$, distributed body forces per unit mass are given by the vector field $\boldsymbol{b}: \mathscr{B} \rightarrow \mathbb{R}^{n_{\text{dim}}}$. The symmetric Cauchy stress and the nonsymmetric deformation gradient together with its determinant are introduced as $\boldsymbol{\sigma}: \mathscr{B} \rightarrow \mathbb{R}^{n_{\text{dim}} \cdot n_{\text{dim}}}$ and $\boldsymbol{F}: \mathscr{B}_0 \rightarrow \mathbb{R}^{n_{\text{dim}} \times n_{\text{dim}}}$ with $J = \det \boldsymbol{F}$. Then the boundary value problem of geometrically nonliner continuum mechanics in the spatial setting

$$\operatorname{div} \boldsymbol{\sigma}^{\mathrm{t}} + \rho \boldsymbol{b} = \boldsymbol{0} \quad \text{in } \mathscr{B}$$

$$\boldsymbol{\sigma} - \boldsymbol{\sigma}^{\mathrm{t}} = \mathbf{0} \quad \text{in } \mathscr{B}$$

$$\boldsymbol{F} - \nabla_X \boldsymbol{\varphi} = \mathbf{0} \quad \text{in } \mathscr{B}_0$$

$$\boldsymbol{\sigma} - J^{-1}\boldsymbol{\tau}(\boldsymbol{F}, \ \ldots, \ ) = \mathbf{0} \quad \text{in } \mathscr{B}$$

$$\boldsymbol{x} - \boldsymbol{x}^{\mathrm{p}} = \mathbf{0} \quad \text{on } \partial\mathscr{B}_x$$

$$\boldsymbol{\sigma}^{\mathrm{t}} \cdot \boldsymbol{n} - \boldsymbol{t}^{\mathrm{p}} = \mathbf{0} \quad \text{on } \partial\mathscr{B}_{\mathrm{t}} \tag{1}$$

consists of the balance of linear momentum in Eq. $(1)_1$, the balance of angular momentum in Eq. $(1)_2$, the kinematic relations defining the deformation gradient in Eq. $(1)_3$, the generic constitutive law for the Kirchhoff stress $\boldsymbol{\tau}$ in Eq. $(1)_4$ together with the Dirichlet and Neumann boundary conditions for the deformation and the spatial traction vector $\boldsymbol{t}$ in Eqs. $(1)_5$ and $(1)_6$.

## 3. Concept of strong discontinuities at large strains

This section is devoted to the kinematic characterization of strong discontinuities. Therefore, we first give a brief account on material surfaces. Then we discuss strong discontinuities across material surfaces and the resulting multiplicative decomposition of the deformation gradient into a singular and a regular part. Finally, strong discontinuities are regularized by substituting the discontinuity surface by a band with small but finite width.

### 3.1. Characterization of material surfaces

As a preliminary to the subsequent discussion, consider the monotonic function $S(\boldsymbol{X})$: $\mathbb{R}^3 \rightarrow \mathbb{R}$ defined on the reference configuration $\mathscr{B}_0$. The material surface $\Gamma_0$ attached to $\mathscr{B}_0$ with unit normal $\boldsymbol{N}_{\mathrm{s}}$, as shown in Fig. 1, is then defined as

$$S(\boldsymbol{X}) = 0 \quad \text{and} \quad \boldsymbol{N}_{\mathrm{s}} = j_0^{-1}\nabla_X S \quad \text{with } j_0 = |\ \nabla_X S\ | \ . \tag{2}$$

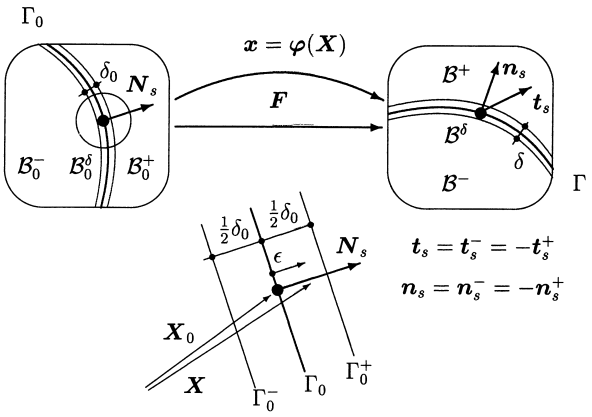


Fig. 1. Regularized discontinuity across a material surface.

The surface subdivides $\mathscr{B}_0$ into $\mathscr{B}_0^-$ and $\mathscr{B}_0^+$ with the unit normal $\boldsymbol{N}_s$ pointing from $\mathscr{B}_0^-$ to $\mathscr{B}_0^+$. During the deformation $\boldsymbol{x}=\boldsymbol{\varphi}(\boldsymbol{X})$ the surface $\Gamma_0$ and the unit normal $\boldsymbol{N}_s$ are convected to the surface $\Gamma$ and the unit normal $\boldsymbol{n}_s$ in the spatial configuration $\mathscr{B}$ via the relations

$$s(\boldsymbol{x})=S(\boldsymbol{\varphi}^{-1}(\boldsymbol{x}))=0 \quad \text{and} \quad \boldsymbol{n}_s=j^{-1}\nabla_x s=\frac{j_0}{j}\boldsymbol{N}_s\cdot\boldsymbol{F}^{-1} \quad \text{with } j=\mid \nabla_x s \mid . \tag{3}$$

**Remark.** Since the surface $\Gamma_0$ is assumed to be attached to $\mathscr{B}_0$, its material time derivative is $\dot{S}=0$, and the convective velocity $c$ of the spatial surface $\Gamma$ is given by $c=j^{-1}\partial_t s=-\boldsymbol{n}_s\cdot\partial_t\boldsymbol{\varphi}$.

### 3.2. Kinematics of strong discontinuities

Next, a possibly discontinuous deformation map $\boldsymbol{\varphi}(\boldsymbol{X})$ that is spatially smooth except across $\Gamma_0$ is expressed as

$$\boldsymbol{\varphi}(\boldsymbol{X})=\boldsymbol{\varphi}_c(\boldsymbol{X})+H_S(\boldsymbol{X})[\![\boldsymbol{\varphi}]\!], \tag{4}$$

with $\boldsymbol{\varphi}_c(\boldsymbol{X})$ the spatially continuous part of the deformation map. Moreover, $H_S(\boldsymbol{X})$ is the Heaviside function centred on $\Gamma_0$, and $[\![\boldsymbol{\varphi}]\!]$ is the jump of $\boldsymbol{\varphi}(\boldsymbol{X})$ across $\Gamma_0$. This jump is locally assumed to be preserved along $\Gamma_0$ in the sense that $[\![\boldsymbol{\varphi}]\!]=\text{const}$ along $\Gamma_0$. Thereby, the jump $[\![\boldsymbol{\varphi}]\!]$ is defined as

$$[\![\boldsymbol{\varphi}]\!]=\lim_{\epsilon\to 0}[\boldsymbol{\varphi}(\boldsymbol{X}_0+\epsilon\boldsymbol{N}_s)-\boldsymbol{\varphi}(\boldsymbol{X}_0-\epsilon\boldsymbol{N}_s)] \quad \text{where } \boldsymbol{X}_0\in\Gamma_0. \tag{5}$$

The Heaviside function $H_S(\boldsymbol{X})$ on $\Gamma_0$ is defined via the function $H(\bullet)$ as

$$H_S(\boldsymbol{X})=H(S(\boldsymbol{X}))=\begin{cases}0 & \text{iff} \quad \boldsymbol{X}\in\mathscr{B}_0^-\\ 1 & \text{iff} \quad \boldsymbol{X}\in\Gamma_0\\ 1 & \text{iff} \quad \boldsymbol{X}\in\mathscr{B}_0^+\end{cases} \quad \text{with } H(\bullet)=\begin{cases}0 & \forall(\bullet)<0\\ 1 & \forall(\bullet)\geq 0\end{cases}. \tag{6}$$

To simplify notation we shall in the sequel omit the arguments of all field quantities if there is no risk of confusion.

In order to obtain the singular deformation gradient associated with $\boldsymbol{\varphi}$ in Eq. (4), the scalar-valued Dirac-delta distribution $\delta_S$ on $\Gamma_0$ is defined via the function $\delta(\bullet)$ as

$$\delta_S=\delta(S(\boldsymbol{X}))=\begin{cases}0 & \text{iff} \quad \boldsymbol{X}\in\mathscr{B}_0^-\\ \infty & \text{iff} \quad \boldsymbol{X}\in\Gamma_0\\ 0 & \text{iff} \quad \boldsymbol{X}\in\mathscr{B}_0^+\end{cases} \quad \text{with } \delta(\bullet)=\begin{cases}\infty & \forall(\bullet)=0\\ 0 & \forall(\bullet)\neq 0\end{cases}. \tag{7}$$

Moreover, the vector-valued Dirac-delta distribution $\boldsymbol{\delta}_S$ and the Heaviside function $H_S$ on $\Gamma_0$ are related in a distributional sense by

$$\int_{\mathscr{B}_0}(\bullet)\cdot\boldsymbol{\delta}_S\,\mathrm{d}V=\int_{\mathscr{B}_0}(\bullet)\cdot\nabla_X H_S\,\mathrm{d}V=\int_{\Gamma_0}(\bullet)\cdot\boldsymbol{N}_s\,\mathrm{d}A \quad \forall(\bullet)\in[C_0^\infty(\mathscr{B}_0)]^{n_{\dim}\,(\bullet)}. \tag{8}$$

The last relation follows from integration by parts while taking into account the definition of $H_S$ and $C_0^\infty(\mathscr{B}_0)$. Therefore, the relation between $\delta_S$ and $H_S$ on $\Gamma_0$ may be stated as the functional identity

$$\nabla_X H_S=\boldsymbol{\delta}_S \quad \text{with } \nabla_X H_S=j_0\delta_S\boldsymbol{N}_s. \tag{9}$$

Since $[\![\boldsymbol{\varphi}]\!]$ is spatially constant along $\Gamma_0$, we may express the material deformation gradient, which is singular along the discontinuity surface, as a multiplicative decomposition into a regular and a singular part

$$\boldsymbol{F} = \boldsymbol{F}_\delta \cdot \boldsymbol{F}_c = \boldsymbol{F}_c + j_0 \delta_S [\![\boldsymbol{\varphi}]\!] \otimes \boldsymbol{N}_s \quad \text{with } \boldsymbol{F}_\delta = \boldsymbol{I} + j \delta_S [\![\boldsymbol{\varphi}]\!] \otimes \boldsymbol{n}_s. \tag{10}$$

Here, $\boldsymbol{F}_c$ denotes the continuous contribution to $\boldsymbol{F}$ and the spatial normal $\boldsymbol{n}_s$ on $\Gamma$ is computed with the regular part of the deformation gradient as

$$\boldsymbol{n}_s = \frac{j_0}{j} \boldsymbol{N}_s \cdot \boldsymbol{F}_c^{-1}. \tag{11}$$

### 3.3. Regularization of strong discontinuities

For a regularization of the singularity terms, we assume that two parallel surfaces $\Gamma_0^-$ and $\Gamma_0^+$ with the same unit normal $\boldsymbol{N}_s$ surround a narrow band-shaped domain $\mathscr{B}_0^\delta$ of width $\delta_0$, see Fig. 1, with

$$\mathscr{B}_0^\delta = \left\{ \boldsymbol{X} = \boldsymbol{X}_0 + \epsilon \boldsymbol{N}_s \mid \boldsymbol{X}_0 \in \Gamma_0, \ -\frac{\delta_0}{2} \leq \epsilon \leq \frac{\delta_0}{2} \right\}. \tag{12}$$

Thereby, $\delta_0$ is much smaller than a typical geometrical length scale of the domain $\mathscr{B}_0$. We may now introduce the regularized Heaviside function $H_R$ and Dirac-delta distribution $\delta_R$ as

$$H_R = \begin{cases} 0 & \text{iff} \quad \boldsymbol{X} \in \mathscr{B}_0^- \\ \frac{1}{2} + \frac{\epsilon}{\delta_0} & \text{iff} \quad \boldsymbol{X} \in \mathscr{B}_0^\delta \\ 1 & \text{iff} \quad \boldsymbol{X} \in \mathscr{B}_0^+ \end{cases} \quad \text{and} \quad \delta_R = \begin{cases} \frac{1}{j_0 \delta_0} & \text{iff} \quad \boldsymbol{X} \in \mathscr{B}_0^\delta \\ 0 & \text{iff} \quad \boldsymbol{X} \notin \mathscr{B}_0^\delta \end{cases}. \tag{13}$$

Moreover, the regularized vector-valued Dirac-delta distribution $\boldsymbol{\delta}_R$ is defined as

$$\boldsymbol{\delta}_R = j_0 \delta_R \boldsymbol{N}_s = \begin{cases} \frac{1}{\delta_0} \boldsymbol{N}_s & \text{iff} \quad \boldsymbol{X} \in \mathscr{B}_0^\delta \\ 0 & \text{iff} \quad \boldsymbol{X} \notin \mathscr{B}_0^\delta \end{cases}. \tag{14}$$

Thereby, the regularized vector-valued Dirac-delta distribution satisfies the following relation

$$\int_{\mathscr{B}_0} (\bullet) \cdot \boldsymbol{\delta}_R \, dV = \frac{1}{\delta_0} \int_{\mathscr{B}_0^\delta} (\bullet) \cdot \boldsymbol{N}_s \, dV \rightarrow \int_{\Gamma_0} (\bullet) \cdot \boldsymbol{N}_s \, dA \quad \text{for } \delta_0 \rightarrow 0. \tag{15}$$

This result also holds for a finite band width $\delta_0$ if we assume that the quantity $(\bullet)$ does not vary across the band.

The regularized $C^0$-continuous deformation $\boldsymbol{\varphi}$ is then expressed in terms of the regularized Heaviside function $H_R$ as

$$\boldsymbol{\varphi} = \boldsymbol{\varphi}_c + H_R [\![\boldsymbol{\varphi}]\!]. \tag{16}$$

It follows immediately that the regularized version of $\boldsymbol{F}$ may be expressed as in Eq. (10) by simply replacing $\delta_S$ with $\delta_R$. Thus, considering the restriction to the band-shaped domain $\mathscr{B}_0^\delta$ renders the regularized $\boldsymbol{F}$, which is discontinuous, as

$$\boldsymbol{F} = \boldsymbol{F}_\delta \cdot \boldsymbol{F}_c = \boldsymbol{F}_c + \frac{1}{\delta_0}[\![\boldsymbol{\varphi}]\!] \otimes \boldsymbol{N}_s \quad \text{with } \boldsymbol{F}_\delta = \boldsymbol{I} + \frac{1}{\delta}[\![\boldsymbol{\varphi}]\!] \otimes \boldsymbol{n}_s. \tag{17}$$

Here we introduced the spatial thickness $\delta$ of the localization band via the relation $j\delta = j_0\delta_0$. Please note again, the multiplicative representation of $\boldsymbol{F}$.

**Remark.** In the small strain limit the linear strain tensor $\boldsymbol{\epsilon} = \nabla_x^{\text{sym}}\boldsymbol{u}$, with $\boldsymbol{u}$ the regularized discontinuous displacement field, splits additively into a continuous and a discontinuous contribution

$$\boldsymbol{\epsilon} = \boldsymbol{\epsilon}_c + \boldsymbol{\epsilon}_\delta \quad \text{with } \boldsymbol{\epsilon}_\delta = \frac{1}{\delta}[[\![\mathbf{u}]\!] \otimes \boldsymbol{n}_s]^{\text{sym}}. \tag{18}$$

Here, the band thickness $\delta$ is considered a constant quantity.

## 4. Weak form of a geometrically nonlinear BVP

As a prerequisite for a finite element discretization the nonlinear boundary value problem has to be reformulated in weak form. Thereby, an additional contribution to the virtual work expression has to be considered if strong discontinuities in the nonlinear deformation map are taken into account. Therefore, we first review the weak form for the case of a continuous deformation map. Then the additional contribution which arises from internal boundaries in the case of strong discontinuities is given.

### 4.1. Continuous deformation map: no strong discontinuities

The balance of linear momentum in Eq. $(1)_1$ and the Neumann boundary conditions in Eq. $(1)_6$ are tested by a virtual displacement $\delta\boldsymbol{\varphi}$ to render the standard virtual work expression

$$G^{\text{ext}} - G^{\text{int}} = 0 \quad \forall \delta\boldsymbol{\varphi} \in [H^1_0(\mathscr{B})]^{n_{\text{dim}}}. \tag{19}$$

Here, the internal and external contributions $G^{\text{int}}$ and $G^{\text{ext}}$ to the virtual work expand into the standard representations in terms of spatial quantities

$$G^{\text{int}} = \int_{\mathscr{B}} \nabla_x \delta\boldsymbol{\varphi} : \boldsymbol{\sigma}\, dv \quad \text{and} \quad G^{\text{ext}} = \int_{\mathscr{B}} \rho\delta\boldsymbol{\varphi} \cdot \boldsymbol{b}\, da + \int_{\partial\mathscr{B}_t} \delta\boldsymbol{\varphi} \cdot \boldsymbol{t}^p\, dv. \tag{20}$$

In the sequel the discretization of these two contributions to the weak form renders the standard finite element formulation.

### 4.2. Discontinuous deformation map: strong discontinuities

In order to account for strong discontinuities let the current domain $\mathscr{B}$ be split by an internal boundary $\Gamma$ with surface normal $\boldsymbol{n}_s$ into the subdomains $\mathscr{B}^+$ and $\mathscr{B}^-$, whereby $\boldsymbol{n}_s = \boldsymbol{n}_s^- = -\boldsymbol{n}_s^+$ points into $\mathscr{B}^+$. Recall that jumps of field quantities $(\bullet)$ across $\Gamma$ are denoted by $[\![(\bullet)]\!] = (\bullet)^+ - (\bullet)^-$. We then conclude that the test function or rather virtual displacement experiences a discontinuity $[\![\delta\boldsymbol{\varphi}]\!]$ across $\Gamma$. Taking into account the traction continuity $\boldsymbol{t}_s = \boldsymbol{t}_s^- = -\boldsymbol{t}_s^+$, compare Fig. 1, we obtain the weak form of the balance of linear momentum in Eq. $(1)_1$ and the Neumann boundary conditions in Eq. $(1)_6$ for the case of an internal boundary as

$$G^{\text{ext}} - G^{\text{int}} - G^{\text{dis}} = 0 \quad \forall \delta\boldsymbol{\varphi} \in [BD_0(\mathscr{B})]^{n_{\text{dim}}} . \tag{21}$$

Thereby, the additional virtual work contribution $G^{\text{dis}}$ due to the discontinuity expressed by spatial quantities follows as

$$G^{\text{dis}} = \int_{\Gamma} [\![\delta\boldsymbol{\varphi}]\!] \cdot \boldsymbol{t}_{\text{s}} \, \text{d}a. \tag{22}$$

Clearly, the standard contributions $G^{\text{int}}$ and $G^{\text{ext}}$ are now defined on each subdomain separately

$$G^{\text{int}} = G^{\text{int}}(\mathscr{B}^-) + G^{\text{int}}(\mathscr{B}^+) \quad \text{and} \quad G^{\text{ext}} = G^{\text{ext}}(\mathscr{B}^-) + G^{\text{ext}}(\mathscr{B}^+). \tag{23}$$

In the sequel the discretization of this extra contribution to the weak form renders the interface finite element formulation.

## 5. Geometrically nonlinear interface constitutive law

In this section we are concerned with the formulation of a constitutive law, which we shall, henceforth, address as the interface constitutive law, for the spatial traction vector $\boldsymbol{t}_{\text{s}}$ transmitted across the discontinuity $\Gamma$. To this end, in addition to the observation that the virtual displacement experiences a discontinuity $[\![\delta\boldsymbol{\varphi}]\!]$ across $\Gamma$, we incorporate the deformation map discontinuity $[\![\boldsymbol{\varphi}]\!]$. Thereby, the key step is the identification of the appropriate structure for the driving quantity for $\boldsymbol{t}_{\text{s}}$, whereby different choices are conceptually possible.

Here we shall extend the geometrically linear proposal by Larsson et al. (1993) to the geometrically nonlinear case. This concept essentially results in a projection of the constitutive behaviour in the continuous neighbouring domain $\mathscr{B}^{\pm}$ into the discontinuity across $\Gamma$.

To this end, motivated by the concept of regularized strong discontinuities above, we postulate that the deformation map jump across $\Gamma$ results in the relative deformation gradient $\boldsymbol{F}_{\delta} = \boldsymbol{F} \cdot \boldsymbol{F}_{\text{c}}^{-1}$ within the regularized discontinuity. Thereby, $\boldsymbol{F}_{\delta}$ is characterized by the dyadic structure of $[\![\boldsymbol{\varphi}]\!]$ and the normal $\boldsymbol{n}_{\text{s}}$ together with the spatial length scale $\delta$

$$\boldsymbol{F}_{\delta} = \boldsymbol{I} + \frac{1}{\delta}[\![\boldsymbol{\varphi}]\!] \otimes \boldsymbol{n}_{\text{s}}. \tag{24}$$

Here, the length $\delta$ might either be interpreted as the regularization parameter within the concept of regularized strong discontinuities or, in view of the discussion above, rather as the current width of the discontinuity. The interface deformation gradient and its inverse are alternatively expressed in terms of the oriented surface element $\text{d}\boldsymbol{a}_{\text{s}} = \boldsymbol{n}_{\text{s}} \, \text{d}a$ and the abbreviations $V_{\delta} = \delta \, \text{d}a$ and $v_{\delta} = V_{\delta} + [\![\boldsymbol{\varphi}]\!] \cdot \text{d}\boldsymbol{a}_{\text{s}}$ as

$$\boldsymbol{F}_{\delta} = \boldsymbol{I} + \frac{1}{V_{\delta}}[\![\boldsymbol{\varphi}]\!] \otimes \text{d}\boldsymbol{a}_{\text{s}} \quad \text{and} \quad \boldsymbol{F}_{\delta}^{-1} = \boldsymbol{I} - \frac{1}{v_{\delta}}[\![\boldsymbol{\varphi}]\!] \otimes \text{d}\boldsymbol{a}_{\text{s}}. \tag{25}$$

Then, the traction vector is a projection of the standard stress response as given by the constitutive law in Eq. $(1)_4$ defined in $\mathscr{B}^{\pm}$ onto the discontinuity across $\Gamma$

$$\boldsymbol{t}_{\text{s}} = J_{\delta}^{-1} \boldsymbol{\tau}(\boldsymbol{F}_{\delta}^{\text{e}}) \cdot \boldsymbol{n}_{\text{s}}, \tag{26}$$

whereby, in the frame of multiplicative elasto-plasticity $\boldsymbol{F}_{\delta}^{\text{e}}$ defined the elastic part of $\boldsymbol{F}_{\delta} = \boldsymbol{F}_{\delta}^{\text{e}} \cdot \boldsymbol{F}_{\delta}^{\text{p}}$.

**Remark.** In the geometrically linear case Larsson et al. (1993) considered $\boldsymbol{\epsilon}_{\delta} = (1/\delta)[[\![\boldsymbol{u}]\!] \otimes \boldsymbol{n}_{\text{s}}]^{\text{sym}}$ as the

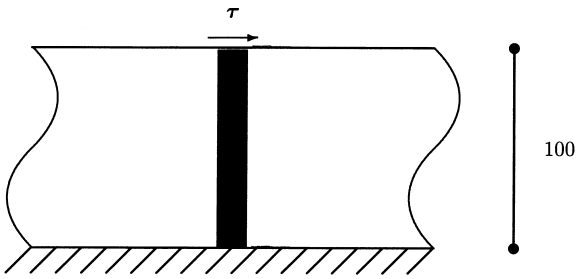


Fig. 2. Softening shear layer at larger strains.

primary kinematic quantity within the regularized discontinuity. Therefore, they proposed to compute the interface traction $\boldsymbol{t}_s$ from the relative strain $\boldsymbol{\epsilon}_\delta = \boldsymbol{\epsilon}_\delta^e + \boldsymbol{\epsilon}_\delta^p$, e.g. for an elasto-plastic material from the projection of $\boldsymbol{\sigma}(\boldsymbol{\epsilon}_\delta^e)$ with the interface normal $\boldsymbol{n}_s$. As a consequence, upon linearization the tangent law for the traction vector involved the second-order localization tensor $\boldsymbol{q}^{ep}$ with $\boldsymbol{q}^{ep} \cdot [\bullet] = [\boldsymbol{\mathscr{E}}^{ep} : [[\bullet] \otimes \boldsymbol{n}_s]] \cdot \boldsymbol{n}_s$, i.e. the double contraction of the elasto-plastic fourth-order tangent operator $\boldsymbol{\mathscr{E}}^{ep}$ with the normal $\boldsymbol{n}_s$, which characterises the localization properties of an elasto-plastic solid. Thereby, for the computation of $\boldsymbol{q}^{ep}$ the contractions with $\boldsymbol{n}_s$ are performed with respect to the second and fourth index of $\boldsymbol{\mathscr{E}}^{ep}$.

## 6. Linearization of the weak form

In this section we consider the linearization of the contribution to the virtual work $G^{dis}$ due to the discontinuity. Thereby, linearizations are denoted like material time derivatives by a superposed dot

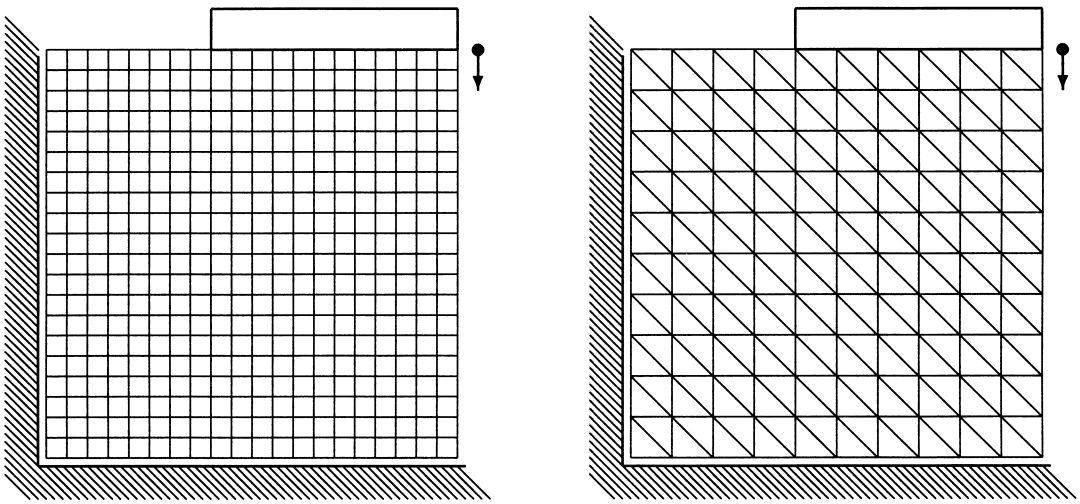

Fig. 3. Geometry and discretizations of chip cutting problem.

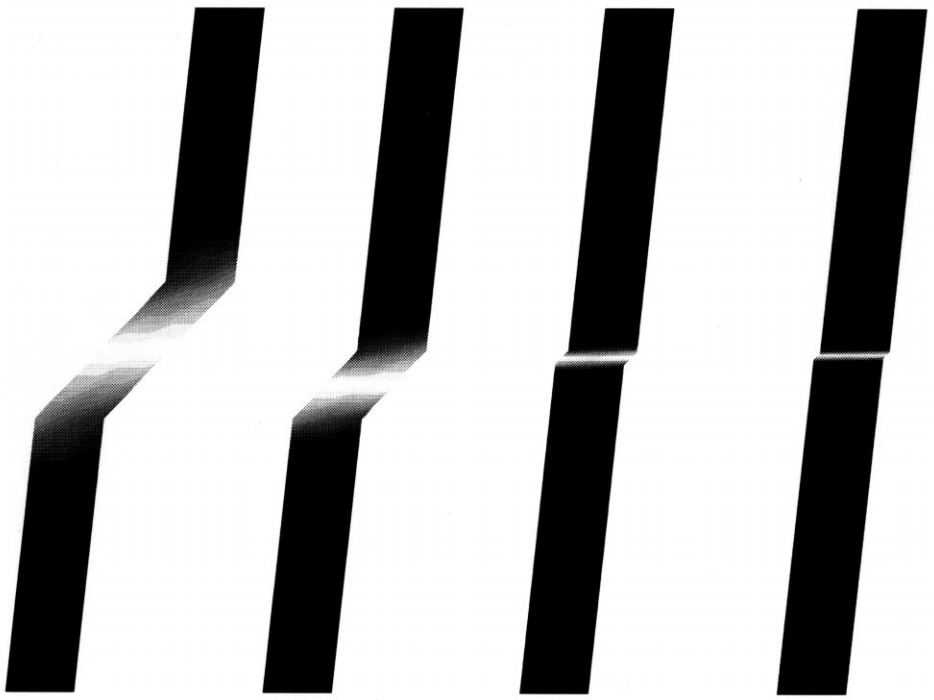

Fig. 4. Deformed configurations and plastic zones for 10, 20 100, 200 $P2$ elements.

$$\dot{G}^{\mathrm{dis}} = \int_{\Gamma} [\![\delta\boldsymbol{\varphi}]\!] \cdot \overline{\dot{\boldsymbol{t}}_{\mathrm{s}}\, \mathrm{d}a} = \int_{\Gamma} [\![\delta\boldsymbol{\varphi}]\!] \cdot \overline{\dot{J}_{\delta}^{-1}\boldsymbol{\tau} \cdot \mathrm{d}\boldsymbol{a}_{\mathrm{s}}} \quad \text{with } \mathrm{d}\boldsymbol{a}_{\mathrm{s}} = \boldsymbol{n}_{\mathrm{s}}\, \mathrm{d}a. \tag{27}$$

The material time derivative of the Kirchhoff stress $\dot{\boldsymbol{\tau}} = \mathscr{E}_2^{\mathrm{ep}} : \boldsymbol{l}_{\delta} + \boldsymbol{\tau} \cdot \boldsymbol{l}_{\delta}^{\mathrm{t}} + \boldsymbol{l}_{\delta} \cdot \boldsymbol{\tau}$ may be expressed in terms of the spatial tangent operator $\mathscr{E}_2^{\mathrm{ep}}$ and correction terms, thus we obtain

$$\overline{\dot{J}_{\delta}^{-1}\boldsymbol{\tau} \cdot \mathrm{d}\boldsymbol{a}_{\mathrm{s}}} = J_{\delta}^{-1}[\mathscr{E}_2^{\mathrm{ep}} : \boldsymbol{l}_{\delta} + \boldsymbol{\tau} \cdot \boldsymbol{l}_{\delta}^{\mathrm{t}}] \cdot \mathrm{d}\boldsymbol{a}_{\mathrm{s}} + [\boldsymbol{l}_{\delta} - [\boldsymbol{l}_{\delta} : \boldsymbol{I}]\boldsymbol{I}] \cdot \boldsymbol{t}_{\mathrm{s}}\, \mathrm{d}a + J_{\delta}^{-1}\boldsymbol{\tau} \cdot \overline{\dot{\mathrm{d}}\boldsymbol{a}_{\mathrm{s}}}. \tag{28}$$

Here, the spatial interface velocity gradient $\boldsymbol{l}_{\delta}$ is based on the interface deformation gradient $\boldsymbol{F}_{\delta}$ and its inverse and follows after tedious algebra by setting $V_{\delta} = \delta\, \mathrm{d}a = \delta_0\, \mathrm{d}A$ as

$$\boldsymbol{l}_{\delta} = \frac{1}{V_{\delta}} [\![\boldsymbol{\varphi}]\!] \otimes \overline{\dot{\mathrm{d}}\boldsymbol{a}_{\mathrm{s}}} + \frac{1}{v_{\delta}} \left[ \overline{\dot{[\![\boldsymbol{\varphi}]\!]}} - \frac{1}{V_{\delta}} [[\![\boldsymbol{\varphi}]\!] \otimes [\![\boldsymbol{\varphi}]\!]] \cdot \overline{\dot{\mathrm{d}}\boldsymbol{a}_{\mathrm{s}}} \right] \otimes \mathrm{d}\boldsymbol{a}_{\mathrm{s}}. \tag{29}$$

The determinant $J_{\delta}$ of the interface deformation gradient together with its linearization are given by

$$J_{\delta} = v_{\delta}/V_{\delta} \quad \text{and} \quad \dot{J}_{\delta} = J_{\delta}\boldsymbol{l}_{\delta} : \boldsymbol{I} = \frac{1}{V_{\delta}} [\mathrm{d}\boldsymbol{a}_{\mathrm{s}} \cdot \overline{\dot{[\![\boldsymbol{\varphi}]\!]}} + [\![\boldsymbol{\varphi}]\!] \cdot \overline{\dot{\mathrm{d}}\boldsymbol{a}_{\mathrm{s}}}]. \tag{30}$$

With these preliminaries at hand we obtain for the contribution of the tangent operator in Eq. (28)

$$J_{\delta}^{-1}[\mathscr{E}_2^{\mathrm{ep}} : \boldsymbol{l}_{\delta}] \cdot \mathrm{d}\boldsymbol{a}_{\mathrm{s}} = \frac{1}{\delta} \boldsymbol{q}_{\varphi}^{\mathrm{ep}} \cdot \overline{\dot{\mathrm{d}}\boldsymbol{a}_{\mathrm{s}}} + \frac{\mathrm{d}a^2}{v_{\delta}} \boldsymbol{q}_2^{\mathrm{ep}} \cdot \left[ \overline{\dot{[\![\boldsymbol{\varphi}]\!]}} - \frac{1}{V_{\delta}} [[\![\boldsymbol{\varphi}]\!] \otimes [\![\boldsymbol{\varphi}]\!]] \cdot \overline{\dot{\mathrm{d}}\boldsymbol{a}_{\mathrm{s}}} \right]$$

where we introduced the abbreviation $\boldsymbol{q}_{\varphi}^{\mathrm{ep}}$ and the spatial localization tensor $\boldsymbol{q}_2^{\mathrm{ep}}$ as the double

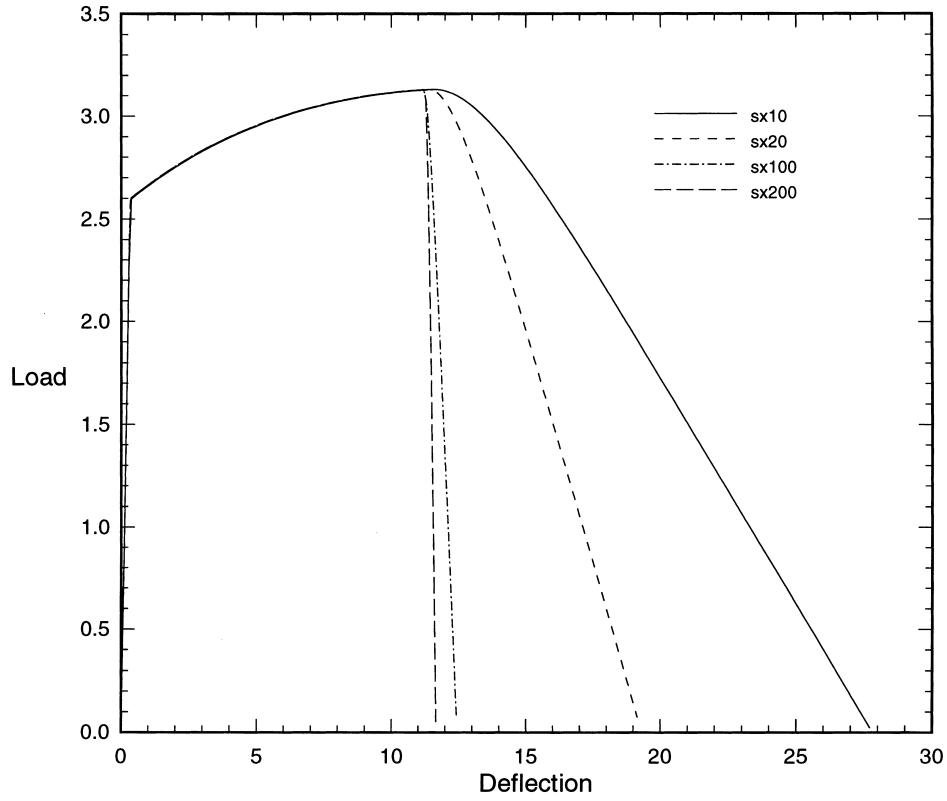


Fig. 5. Load–deflection curves for 10, 20, 100, 200 $P2$ elements.

contraction of the tangent operator $\mathscr{E}_2^{\mathrm{ep}}$

$$J_\delta \boldsymbol{q}_\varphi^{\mathrm{ep}} \cdot [\bullet] = [\mathscr{E}_2^{\mathrm{ep}} : [[\![\boldsymbol{\varphi}]\!] \otimes [\bullet]]] \cdot \boldsymbol{n}_{\mathrm{s}} \quad \text{and} \quad J_\delta \boldsymbol{q}_2^{\mathrm{ep}} \cdot [\bullet] = [\mathscr{E}_2^{\mathrm{ep}} : [[\bullet] \otimes \boldsymbol{n}_{\mathrm{s}}]] \cdot \boldsymbol{n}_{\mathrm{s}}. \tag{31}$$

Thereby, for the computation of $\boldsymbol{q}_\varphi^{\mathrm{ep}}$ the contractions with $\boldsymbol{n}_{\mathrm{s}}$ and $[\![\boldsymbol{\varphi}]\!]$ are performed with respect to the second and third index of $\mathscr{E}_2^{\mathrm{ep}}$, for the computation of $\boldsymbol{q}_2^{\mathrm{ep}}$ the double contraction with $\boldsymbol{n}_{\mathrm{s}}$ is performed with respect to the second and fourth index of $\mathscr{E}_2^{\mathrm{ep}}$. Next, the second term in eq. (28) is expanded into

$$J_\delta^{-1} \boldsymbol{\tau} \cdot \boldsymbol{l}_\delta^{\mathrm{t}} \cdot \mathrm{d}\boldsymbol{a}_{\mathrm{s}} = \frac{\mathrm{d}a}{v_\delta} \left[ [\boldsymbol{t}_{\mathrm{s}} \otimes \mathrm{d}\boldsymbol{a}_{\mathrm{s}}] \cdot \dot{\overline{[\![\boldsymbol{\varphi}]\!]}} + \left[ [\![\boldsymbol{\varphi}]\!] \cdot \boldsymbol{n}_{\mathrm{s}} \boldsymbol{\tau} + \frac{V_\delta - v_\delta}{V_\delta} \boldsymbol{t}_{\mathrm{s}} \otimes [\![\boldsymbol{\varphi}]\!] \right] \cdot \dot{\overline{\mathrm{d}\boldsymbol{a}_{\mathrm{s}}}} \right].$$

Moreover, with the normal Cauchy stress $\sigma_{\mathrm{s}} = \boldsymbol{n}_{\mathrm{s}} \cdot \boldsymbol{t}_{\mathrm{s}}$ acting on the interface we compute

$$\boldsymbol{l}_\delta \cdot \boldsymbol{t}_{\mathrm{s}} \, \mathrm{d}a = \frac{1}{\delta} [[\![\boldsymbol{\varphi}]\!] \otimes \boldsymbol{t}_{\mathrm{s}}] \cdot \dot{\overline{\mathrm{d}\boldsymbol{a}_{\mathrm{s}}}} + \frac{\mathrm{d}a^2}{v_\delta} \sigma_{\mathrm{s}} \left[ \dot{\overline{[\![\boldsymbol{\varphi}]\!]}} - \frac{1}{V_\delta} [[\![\boldsymbol{\varphi}]\!] \otimes [\![\boldsymbol{\varphi}]\!]] \cdot \dot{\overline{\mathrm{d}\boldsymbol{a}_{\mathrm{s}}}} \right].$$

Likewise, the next term in Eq. (28) is represented as

$$-[\boldsymbol{l}_\delta : \boldsymbol{I}] \boldsymbol{t}_{\mathrm{s}} \, \mathrm{d}a = -\frac{\mathrm{d}a}{v_\delta} [[\boldsymbol{t}_{\mathrm{s}} \otimes \mathrm{d}\boldsymbol{a}_{\mathrm{s}}] \cdot \dot{\overline{[\![\boldsymbol{\varphi}]\!]}} + [\boldsymbol{t}_{\mathrm{s}} \otimes [\![\boldsymbol{\varphi}]\!]] \cdot \dot{\overline{\mathrm{d}\boldsymbol{a}_{\mathrm{s}}}}].$$

Finally, combining all terms in Eq. (28) and abbreviating the spatial localization tensor into

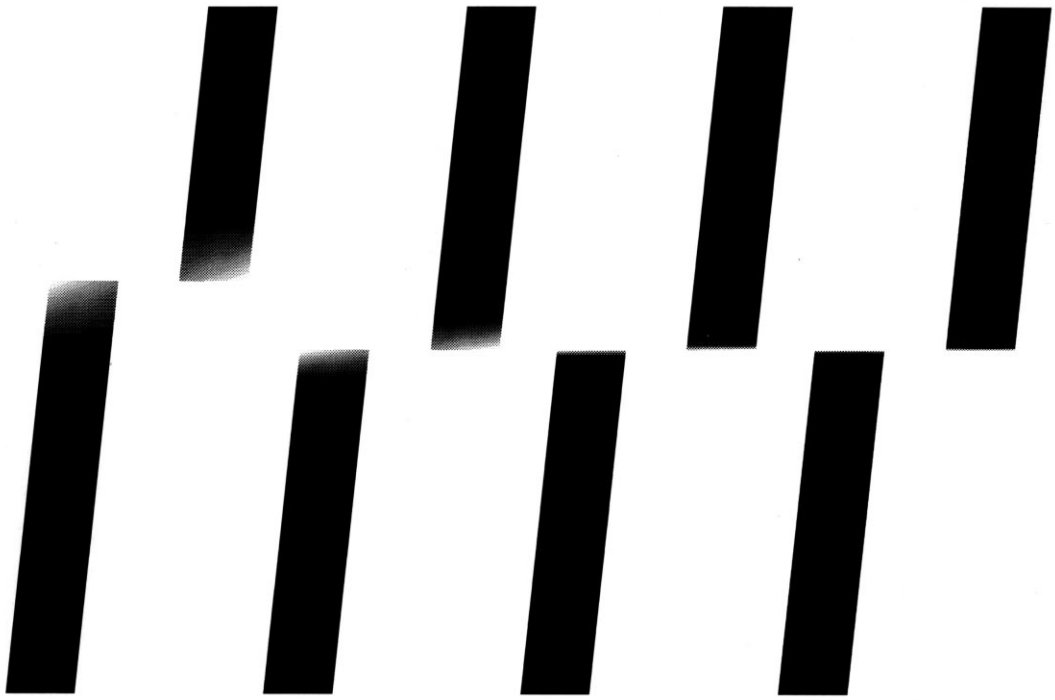

Fig. 6. Deformed configurations and plastic zones for 10, 20, 100, 200 $P2$ (and 1 $I1$) elements $\delta_0 = 20$.

$\boldsymbol{q}_1^{\mathrm{ep}} = \boldsymbol{q}_2^{\mathrm{ep}} + \sigma_{\mathrm{s}}\boldsymbol{I}$ renders the stiffness contribution

$$\overset{\cdot}{\boldsymbol{t}_{\mathrm{s}}}\,\mathrm{d}a = \frac{\mathrm{d}a^2}{v_\delta}\boldsymbol{q}_1^{\mathrm{ep}} \cdot \overset{\cdot}{[\![\boldsymbol{\varphi}]\!]} + \frac{1}{\delta}\left[\boldsymbol{\tau}\delta + 2[[\![\boldsymbol{\varphi}]\!] \otimes \boldsymbol{t}_{\mathrm{s}}]^{\mathrm{skw}} + \boldsymbol{q}_{\varphi}^{\mathrm{ep}} - \frac{\mathrm{d}a}{v_\delta}\boldsymbol{q}_1^{\mathrm{ep}} \cdot [[\![\boldsymbol{\varphi}]\!] \otimes [\![\boldsymbol{\varphi}]\!]]\right] \cdot \overset{\cdot}{\mathrm{d}\boldsymbol{a}_{\mathrm{s}}} \tag{32}$$

which is divided into increments of the deformation map jump $[\![\boldsymbol{\varphi}]\!]$ and the vector valued area element $\mathrm{d}\boldsymbol{a}_{\mathrm{s}}$ of the interface. Thus, the interface stiffness proves to be essentially characterized by the spatial localization tensor $\boldsymbol{q}_1^{\mathrm{ep}}$ and the correction terms to account for a changing $\mathrm{d}\boldsymbol{a}_{\mathrm{s}}$.

## 7. Spatial discretization of the weak form

For the spatial discretization of the interface element we resort to the isoparametric concept. Thereby, the geometry of the interface element, e.g. in the spatial setting $\mathscr{B}$, is a $m_{\mathrm{dim}}$-dimensional Riemannian manifold $\Gamma$ embedded in $\mathbb{R}^{n_{\mathrm{dim}}}$ with $m_{\mathrm{dim}} = n_{\mathrm{dim}} - 1$ and is mapped from the isoparametric domain of dimension $m_{\mathrm{dim}}$ to the physical space by $\boldsymbol{x} = \boldsymbol{x}^{\mathrm{h}}(\xi)$: $[-1, 1]^{m_{\mathrm{dim}}} \rightarrow \mathbb{R}^{n_{\mathrm{dim}}}$. Then the covariant spatial base vectors, i.e. the tangent vectors to the isoparametric coordinate lines, are given as $\boldsymbol{g}_\alpha = \boldsymbol{x}^{\mathrm{h}}_{,\xi\alpha}$ together with the covariant spatial metric coefficients $g_{\alpha\beta} = \boldsymbol{g}_\alpha \cdot \boldsymbol{g}_\beta$ with $\alpha, \beta = 1, \ldots, m_{\mathrm{dim}}$. As a consequence, the infinitesimal length or area elements in the isoparametric domain $[-1, 1]^{m_{\mathrm{dim}}}$ are mapped to $\Gamma$ by $j^{\mathrm{h}} = \sqrt{\det[g_{\alpha\beta}]}$. Accordingly, the geometry in $\mathscr{B}_0$ is characterized by $\boldsymbol{G}_\alpha = \boldsymbol{X}^{\mathrm{h}}_{,\xi\alpha}$, $G_{\alpha\beta} = \boldsymbol{G}_\alpha \cdot \boldsymbol{G}_\beta$ and $J_0^{\mathrm{h}} = \sqrt{\det[G_{\alpha\beta}]}$.

Without loss of generality we consider in the sequel the case of a one-dimensional line interface within a two-dimensional ambient space. Here, the geometry is described by shape functions $N^k(\xi)$

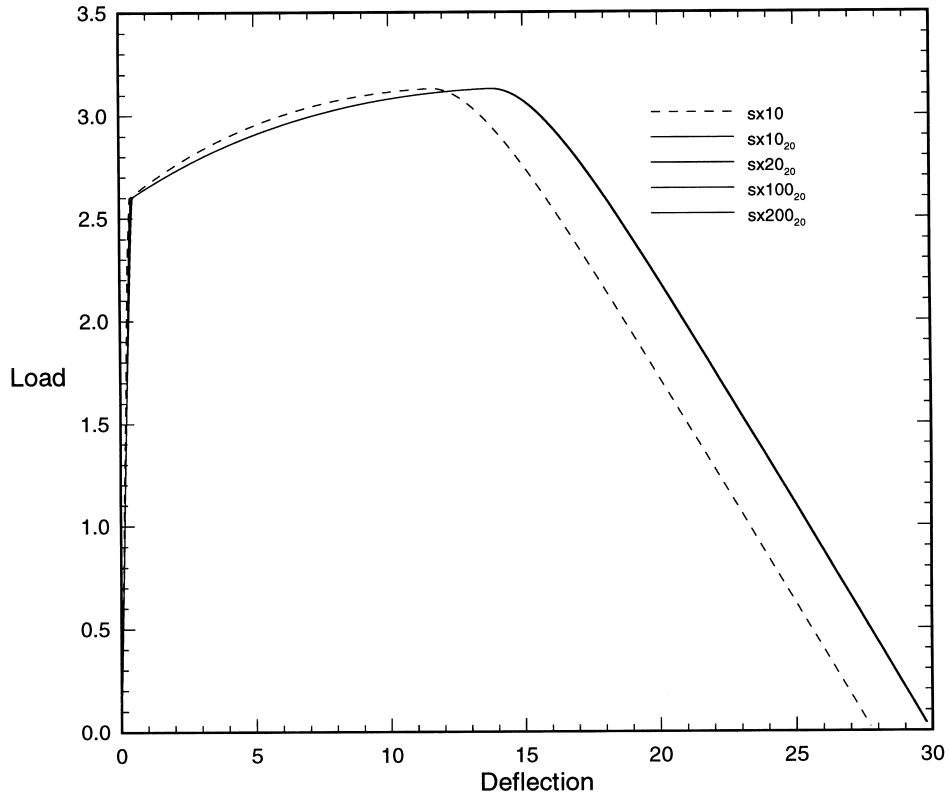


Fig. 7. Load–deflection curves for 10, 20, 100, 200 $P2$ (and 1 $I1$) elements $\delta_0 = 20$.

interpolating the reference and the current node point coordinates $\boldsymbol{X}_k$ and $\boldsymbol{x}_k$, thus in particular the spatial covariant base vector $\boldsymbol{g}_1$ and the corresponding Jacobian $j^{\mathrm{h}}$ follow as

$$\boldsymbol{X}^{\mathrm{h}} = \sum_{k=1}^{nen} N^k \boldsymbol{X}_k, \quad \boldsymbol{x}^{\mathrm{h}} = \sum_{k=1}^{nen} N^k \boldsymbol{x}_k \Longrightarrow \boldsymbol{g}_1 = \sum_{k=1}^{nen} N^k_{,\xi} \boldsymbol{x}_k \quad \text{and} \quad j^{\mathrm{h}} = \sqrt{g_{11}}. \tag{33}$$

Moreover, the same expansions are selected for the approximations to the deformation map jump and its variation

$$[\![\boldsymbol{\varphi}]\!]^{\mathrm{h}} = \sum_{k=1}^{nen} N^k [\![\boldsymbol{\varphi}]\!]_k \quad \text{and} \quad [\![\delta\boldsymbol{\varphi}]\!]^{\mathrm{h}} = \sum_{k=1}^{nen} N^k [\![\delta\boldsymbol{\varphi}]\!]_k. \tag{34}$$

Consequently, the spatial normal $\boldsymbol{n}_{\mathrm{s}}$ to the interface and the spatial area element $\mathrm{d}a$ are simply expressed as

$$\boldsymbol{n}_{\mathrm{s}} = \frac{1}{j^{\mathrm{h}}} \boldsymbol{e}_3 \times \boldsymbol{g}_1 \quad \text{and} \quad \mathrm{d}a = j^{\mathrm{h}}\, \mathrm{d}\xi \Longrightarrow \mathrm{d}\boldsymbol{a}_{\mathrm{s}} = \boldsymbol{e}_3 \times \boldsymbol{g}_1\, \mathrm{d}\xi. \tag{35}$$

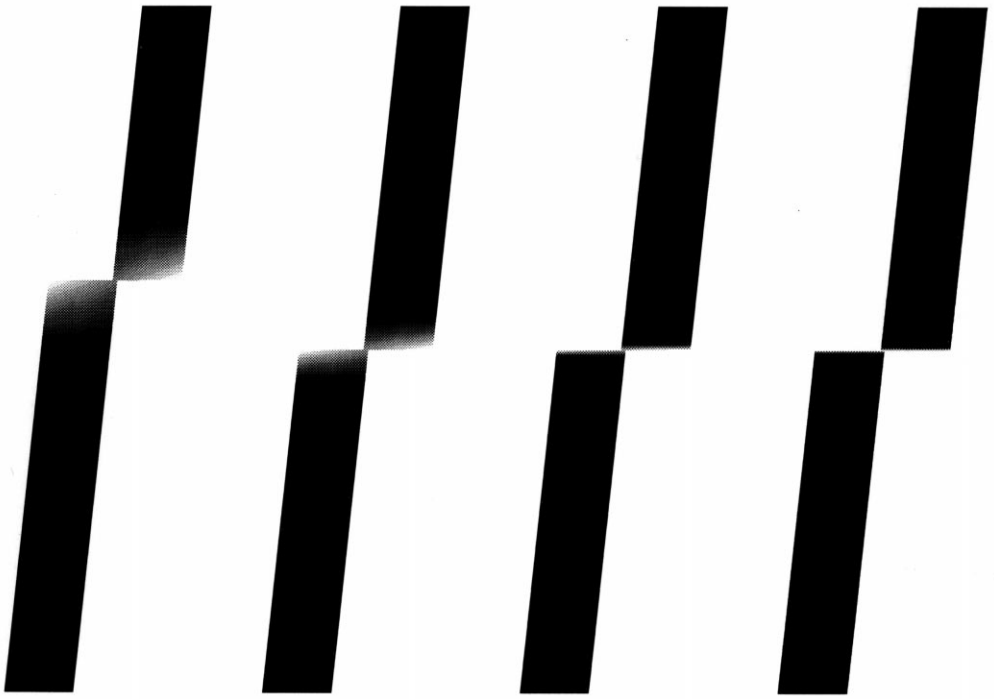

Fig. 8. Deformed configurations and plastic zones for 10, 20, 100, 200 $P2$ (and 1 $I1$) elements $\delta_0 = 10$.

The current regularization parameter is computed from $\delta = \delta_0 j_0^{\mathrm{h}}/j^{\mathrm{h}}$ and the linearized increments of the deformation map jump $[\![\boldsymbol{\varphi}]\!]$ and the vector valued area element $\mathrm{d}\boldsymbol{a}_{\mathrm{s}}$ follow as

$$\dot{\overline{[\![\boldsymbol{\varphi}]\!]}} = \sum_{k=1}^{nen} N^k \dot{\overline{[\![\boldsymbol{\varphi}]\!]}}_k \quad \text{and} \quad \dot{\overline{\mathrm{d}\boldsymbol{a}_{\mathrm{s}}}} = \sum_{k=1}^{nen} N^k_{,\xi} \boldsymbol{e}_3 \times \dot{\boldsymbol{x}}_k \, \mathrm{d}\xi. \tag{36}$$

**Remark.** The extension to a two-dimensional surface interface within a three-dimensional ambient space is straightforward. In particular, the spatial normal $\boldsymbol{n}_{\mathrm{s}}$ and the linearization of the vector valued area element $\mathrm{d}\boldsymbol{a}_{\mathrm{s}}$ are given by

$$\boldsymbol{n}_{\mathrm{s}} = \frac{1}{j^{\mathrm{h}}} \boldsymbol{g}_1 \times \boldsymbol{g}_2 \Longrightarrow \dot{\overline{\mathrm{d}\boldsymbol{a}_{\mathrm{s}}}} = \sum_{k=1}^{nen} [N^k_{,\xi_2} \boldsymbol{g}_1 - N^k_{,\xi_1} \boldsymbol{g}_2] \times \dot{\boldsymbol{x}}_k \, \mathrm{d}\xi_1 \, \mathrm{d}\xi_2.$$

## 8. Localization capturing FE-procedure

In the following we sketch a three step, model adaptive, procedure to capture localization within the frame of a regularized deformation map discontinuity at large inelastic strains which incorporates the

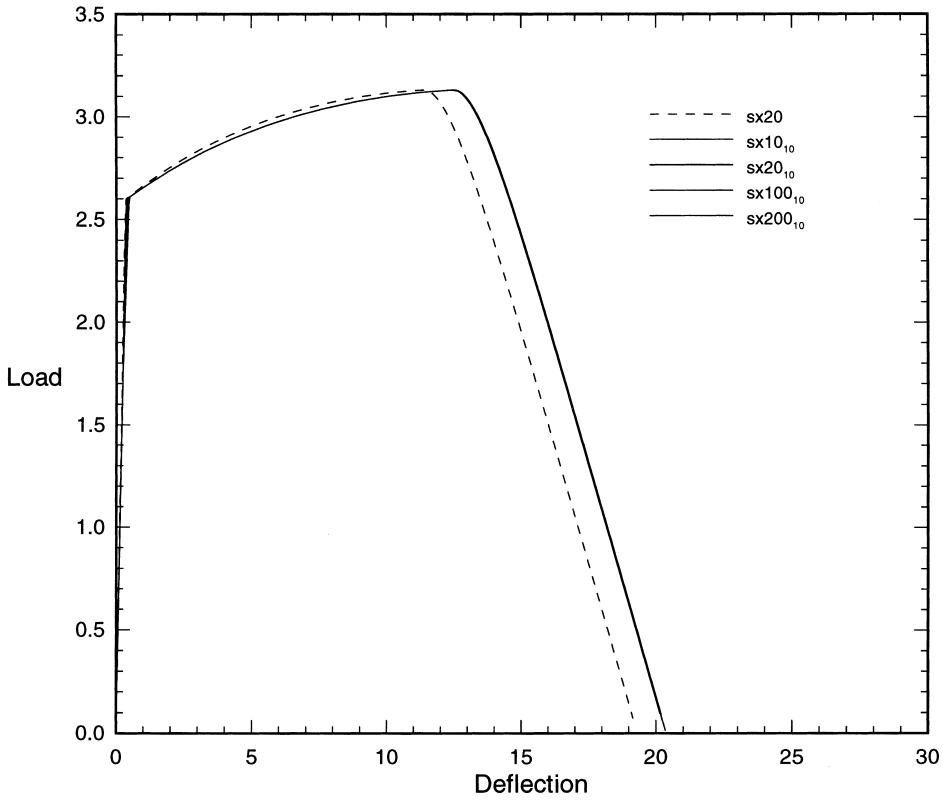


Fig. 9. Load–deflection curves for 10, 20, 100, 200 $P2$ (and 1 $I1$) elements $\delta_0 = 10$.

interface element formulation proposed above. This type of procedure was originally proposed and described in detail by Larsson (1995) for the geometrically linear case. Thereby, the three steps consist of:

1. First we carry out a computation based on an unbiased, possibly homogeneous discretization with our favourite element expansions, e.g. biquadratic $Q2$ quads, without any a priori information about the orientation of a possible localization band. From a mesh densification study and the pointwise diagnosis of the localization tensor we make sure that the problem at hand renders pathological mesh dependent solutions. Moreover, we extract the global placement and orientation of the resolved localization band.
2. Based on the a posteriori information gained from Step 1 we set up an adapted mesh were the element edges are aligned with the localization band. Obviously, for the case of curved discontinuities this task demands a powerful mesh generator, for example based on a pavement strategy, which is able to take into account internal boundaries, see Larsson (1995). Nevertheless, this is a technical issue which shall not be addressed in this work. In the following examples we invoke quadratic triangular $P2$ element which are here mainly suggested by the geometry of the planar solution domain under consideration. Clearly, there are no conceptual restrictions with respect to the element choice. Then, in Step 2, a recalculation of the problem based on the aligned mesh typically renders results where the localization band is resolved with a width spanning over one element row. Again a mesh densification study together with the pointwise diagnosis of the localization tensor reveals the

Fig. 10. Deformed configurations and plastic zones for 10, 20, 100, 200 $P2$ (and 1 $I1$) elements $\delta_0 = 2$.

pathological mesh dependence due to, e.g. in the quasi-static case, the underlying loss of ellipticity.

3. Finally, we apply the concept alluded to above in order to account for regularized deformation map discontinuities at large inelastic strains in the solution. To this end, interface elements containing a regularized deformation map discontinuity with reference width $\delta_0$ are incorporated into the aligned mesh along the resolved localization band. Recall that the interface constitutive law is a projection of the constitutive behaviour in the ambient continuous domain onto the discontinuity. The recalculation of the problem in this step renders a mesh independent solution which is governed by the reference regularization parameter $\delta_0$ and enjoys the characteristics of a true discontinuity. Please note that Step 3 characterizes indeed, a model change from a continuous to a discontinuous solution.

## 9. Examples

In the following examples the isotropic hyperelasto-plastic material is assumed to obey the von Mises yield condition, which incorporates saturation-type hardening, and associated flow and hardening rules of multiplicative hyperelasto-plasticity together with a logarithmic hyperelastic response:

$$\Phi(\boldsymbol{\tau}, \kappa) = \mid \operatorname{dev} \boldsymbol{\tau} \mid -\sqrt{\frac{2}{3}}[Y_0 + [Y_\infty - Y_0][1 - \exp(-m\kappa)] + H\kappa]$$

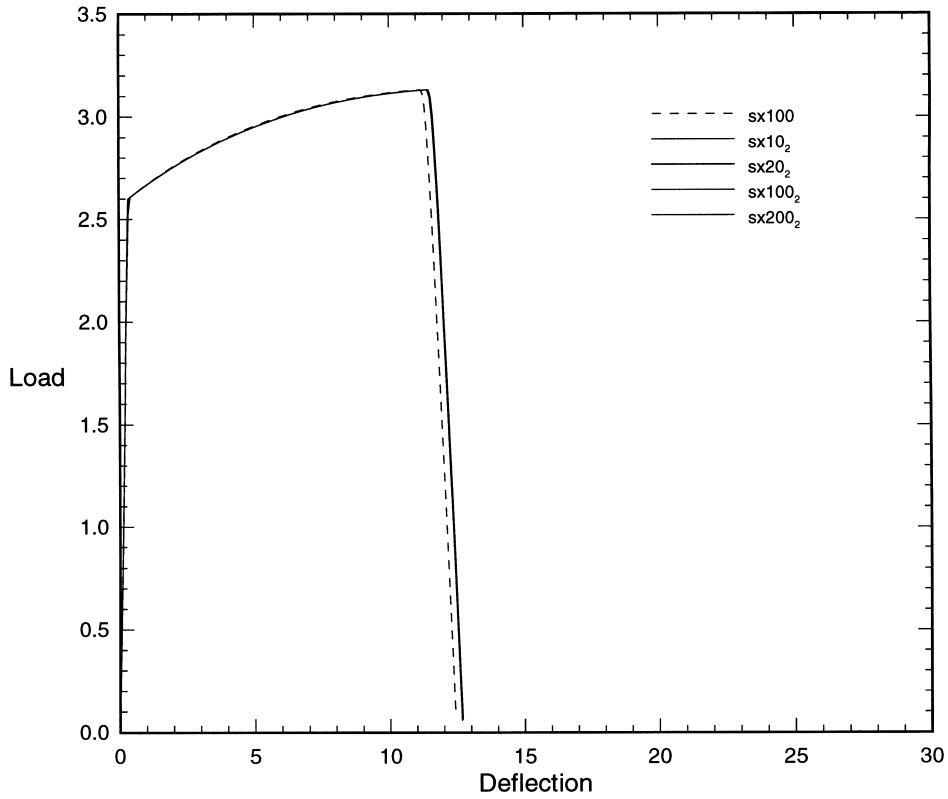


Fig. 11. Load–deflection curves for 10, 20, 100, 200 $P2$ (and 1 $I1$) elements $\delta_0 = 2$.

$$\overline{[\boldsymbol{F}^{\mathrm{p}}]^{\mathrm{t}} \cdot \boldsymbol{F}^{\mathrm{p}}} = \gamma \boldsymbol{F}^{\mathrm{t}} \cdot \frac{\partial \Phi}{\partial \boldsymbol{\tau}} \cdot [\boldsymbol{F}^{\mathrm{e}}]^{-\mathrm{t}} \cdot \boldsymbol{F}^{\mathrm{p}} \quad \text{and} \quad \dot{\kappa} = \sqrt{\frac{2}{3}}\gamma$$

$$\boldsymbol{\tau} = K \ \ln \ J^{\mathrm{e}} \boldsymbol{I} + G \ \mathrm{dev} \ \ln(\boldsymbol{F}^{\mathrm{e}} \cdot [\boldsymbol{F}^{\mathrm{e}}]^{\mathrm{t}}).$$

The flow and hardening rule are integrated implicity by the exponential map and the Euler backward integrator, respectively. The consistent algorithmic tangent operator is invoked to ensure quadratic rate of convergence for the global Newton equilibrium iterations.

### 9.1. Localization in an infinite shear layer

First we consider the infinite shear layer in Fig. 2, in order to study the influence of the regularization parameter $\delta_0$ and the mesh spacing. To this end a shear layer of height $h = 100$ mm (and computational width 10 mm) is discretized into 10, 20, 100 and 200 triangular $P2$ elements with quadratic expansions. Correspondingly, one element row has a height of 20, 10, 2 and 1 mm. The lateral boundary conditions are set such that an infinite layer is modelled. The quasi-static shear force loading is applied to the top surface by arclength control until the load carrying capacity is completely exhausted.

The material parameters are selected as: bulk modulus $K = 164.21$ kN/mm$^2$, shear modulus $G = 80.19$ kN/mm$^2$, initial and saturation yield stress $Y_0 = 0.450$ kN/mm$^2$ and $Y_\infty = 0.715$ kN/mm$^2$, exponential hardening modulus $m = 16.93$ and linear softening modulus $H = -1.2924$ kN/mm$^2$. Here, in addition to

Fig. 12. Deformed configurations and plastic zones for 10, 20, 100, 200 $P2$ (and 1 $I1$) elements $\delta_0 = 1$.

saturation-type hardening, linear softening behaviour is incorporated as a phenomenological description of damage effects.

For the discretization in only continuous $P2$ elements without incorporation of an interface element, where localization is triggered by reducing the initial yield strength in one element row to $Y_0 = 0.445$ kN/mm$^2$. The resulting deformed configurations and the distributions of the hardening variable $\kappa$ are presented in Fig. 4 for the sequence of refined meshes. The corresponding shear load–deflection curves are given in Fig. 5. It is clearly visible that finer meshes render steeper post-peak responses together with narrowing shear band widths. Thereby, due to the perfect alignment of the element edges with the localization zone, the shear band is resolved by only one element row.

Next an $I2$ interface element is introduced into the discretization and the reference regularization parameter is initially set to $\delta_0 = 20$ mm which corresponds to the coarsest mesh spacing of the previous continuous computations into 10 elements. The resulting deformed configurations are shown in Fig. 6 for computations with the sequence of refined meshes. The corresponding shear load–deflection curves are given in Fig. 7. Apparently, the response is completely unaffected by the mesh spacing, moreover, the post-peak response coincides basically with the slope of the load–deflection curve of that continuous computation where the mesh spacing corresponds with $\delta_0$. Nevertheless, since the plastic zones do not occupy the same volume of the specimen for the continuous and the discontinuous discretization, the peaks of the shear load–deflection curves do not agree. The plastic zone localizes completely in the interface elements. Therefore, it would be invisible. Nevertheless, Fig. 6 displays the hardening variable after projection to the neighbouring continuum elements.

The respective results for computations with $\delta_0 =$ 10, 2 and 1 mm corresponding to the mesh spacing of continuous discretizations into 20, 100 and 200 triangular $P2$ elements are given in Figs. 8–13. These results underline again that the response of the discontinuous discretization is completely unaffected by

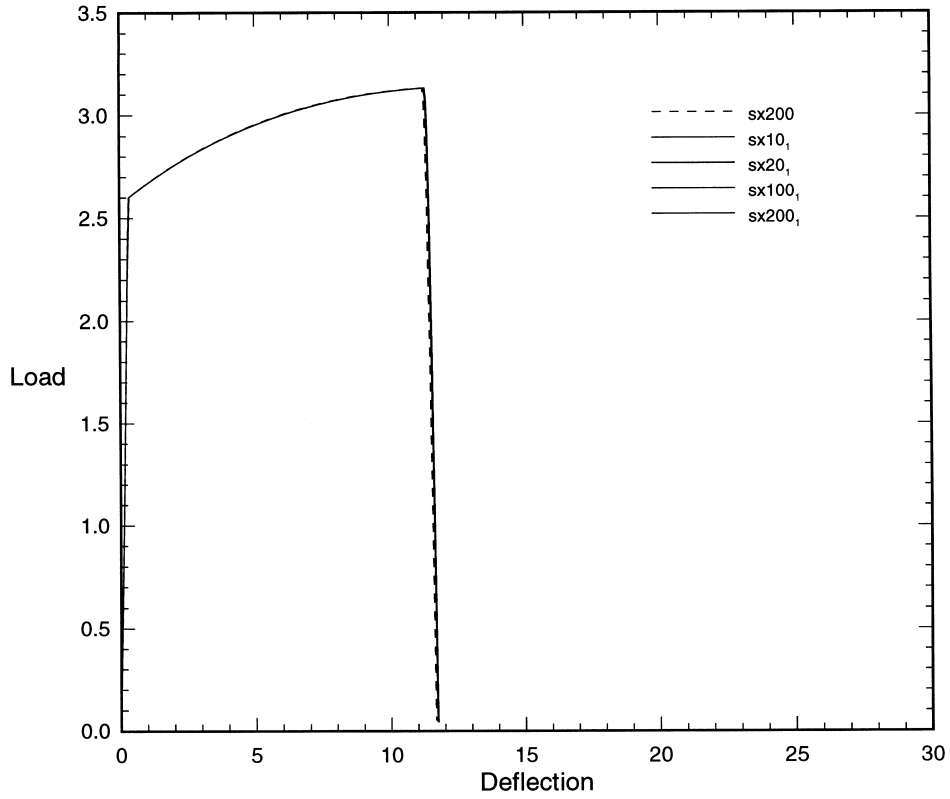


Fig. 13. Load–deflection curves for 10, 20, 100, 200 $P2$ (and 1 $I1$) elements $\delta_0 = 1$.

the surrounding mesh spacing. Likewise, the post-peak response agrees essentially with the slope of the shear load–deflection curve of that continuous computation where the mesh spacing corresponds with $\delta_0$. For small $\delta_0$ even the peaks of the shear load–deflection curves coincide for the continuous and the discontinuous discretization, since then the plastic zones occupy roughly the same volume of the specimen.

### 9.2. Cutting a chip from a square

The next example demonstrates the model adaptive strategy for a representative plane strain BVP, whereby a square panel is loaded by a rigid tool such that a triangular chip is cut (see Fig. 3). The homogeneous square panel has a side length of $l = 10$ mm, the rigid tool spans over 6 mm at the right part of the top surface. The loading is applied quasi-statically to the rigid tool by displacement control until a maximum displacement of 1 mm is obtained.

The material parameters are selected as: bulk modulus $K = 164.21$ kN/mm$^2$, shear modulus $G = 80.19$ kN/mm$^2$, initial and saturation yield stress $Y_0 = Y_\infty = 0.45$ kN/mm$^2$ and linear softening modulus $H = -0.12924$ kN/mm$^2$. These material constants incorporate a linear softening behaviour into the constitutive description as a phenomenological model of damage effects.

In Step 1 we start the calculation with homogeneous discretizations invoking the $Q2$ bilinear element expansion. Fig. 14 shows the deformed configuration and the distribution of the hardening variable $\kappa$ at the end of the loading history for a computation with $20 \times 20$ elements. Typically for a localization

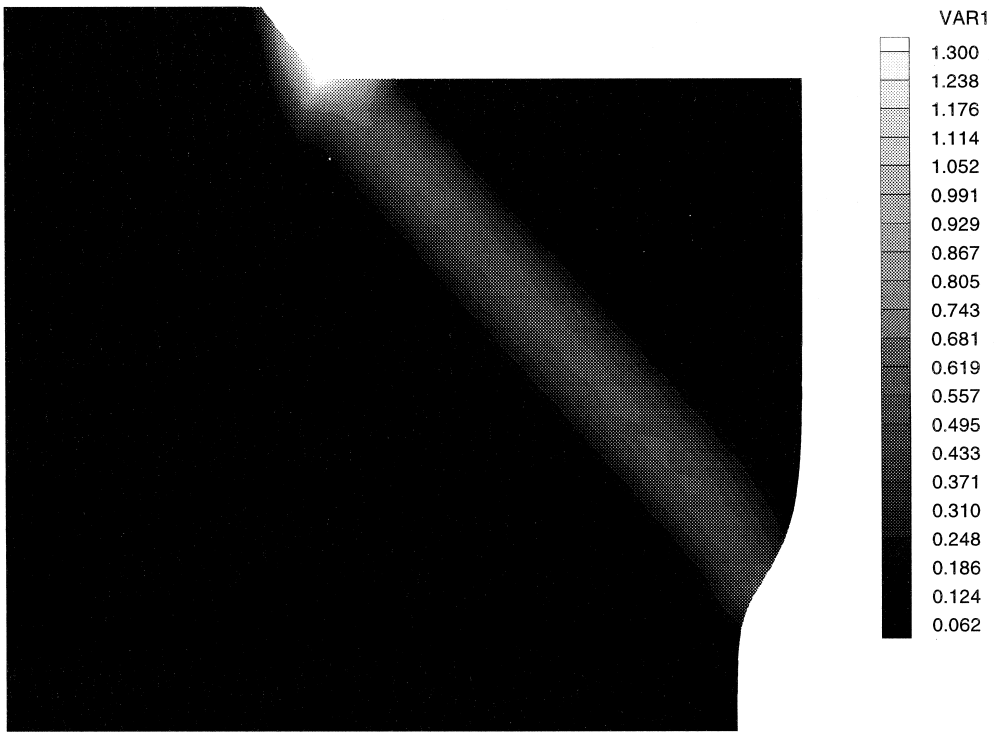


Fig. 14. Deformed configuration and plastic zone $20 \times 20$ $Q2$ discretization.

problem, the plastic zone indicates the pronounced accumulation of inelastic strains in a narrow band. Thereby, a mesh densification study proves the decrease of the resolved shear band width and the increase of the total amount of plastic strain within the band as mesh spacing is reduced. Apparently, the upper triangular part of the specimen tends to move more or less like a rigid body. Nevertheless, this failure mode is not fully developed due to the continuous discretization of the deformation map.

Next due to the simple geometry of the predicted localization band in Step 1, the mesh alignment in Step 2 is favourably accomplished by triangular $P2$ element expansions with a $10 \times 10$ discretization corresponding to 200 elements. It is well-known that aligned meshes are able to capture a narrow localization band (see Steinmann and Willam, 1994) which here is neatly reflected by the distribution of the hardening variable $\kappa$ and the deformed configuration in Fig. 15. Fig. 15 also clearly highlights the development of a failure mode with the minimum localization band width resolvable by the given discretization, i.e. one element row. Thus, mesh refinement would render pathological mesh dependence with respect to the localization band width and consequently with respect to the overall load carrying capacity.

Finally, in Step 3, the additional interface $I2$ elements with quadratic expansions are incorporated into the discretization along the resolved shear band. Here, the reference value of the regularization parameter is set to $\delta_0 = l/100$. Obviously, this step changes the underlying model assumption to the possibility of true discontinuities in the deformation map as demonstrated for the deformed configuration in Fig. 16. Now the solution domain is truly split into two parts sliding almost rigidly along the discontinuity. Thereby, the resulting plastic zone, plotted in Fig. 16 after projection to the

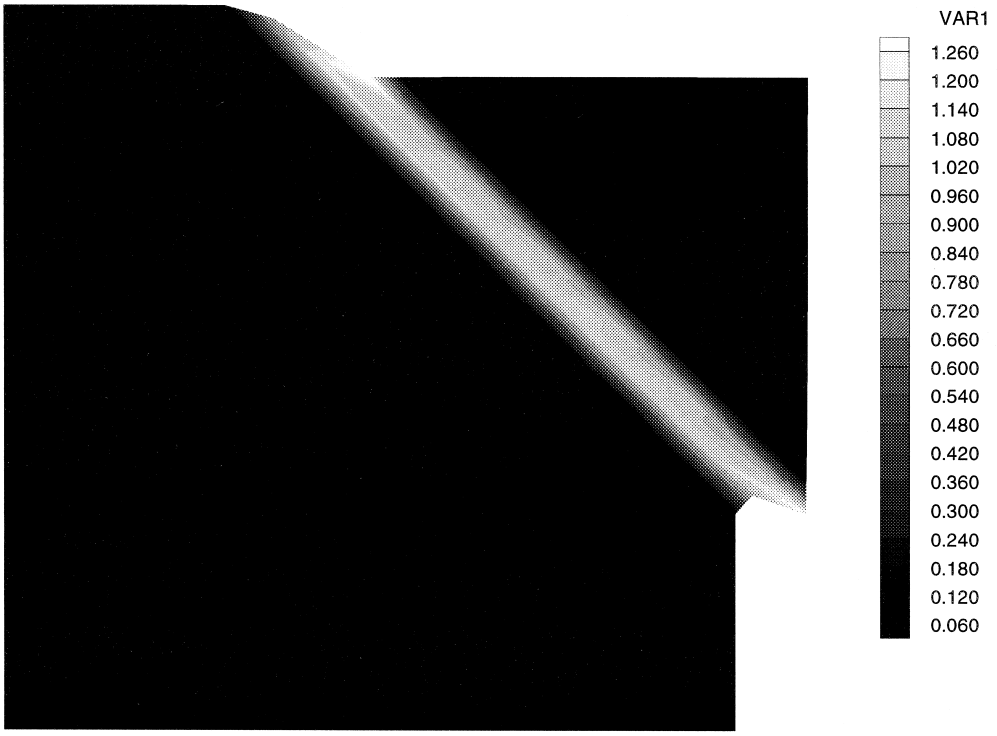


Fig. 15. Deformed configuration and plastic zone $10 \times 10$ $P2$ discretization.

neighbouring continuum elements, localizes completely in the interface elements with a tremendous total amount for the hardening variable $\kappa$.

## 10. Summary

The objective of this work has been the development of a finite element interface formulation capable of capturing localization in geometrically nonlinear solid mechanics. Thereby, it is understood that strong discontinuities characterize the final failure mechanism within localization problems.

The essential ingredient of the proposed formulation is the incorporation of the failure kinematics, which are here governed by the jump in the nonlinear deformation map along the discontinuity, into the finite element formulation. As one possibility for a suitable finite element discretization an interface element, which has to be aligned a priori with the anticipated localization band in the finite element mesh, is endowed with these failure kinematics. Interestingly enough, it turns out that the resulting interface stiffness is dominated by the weighted spatial localization tensor. Guided by the above developments a three step, model adaptive procedure based on the concept of regularized strong discontinuities is motivated and is applied to localization computations. The results neatly indicate the applicability of the concept advocated in this contribution.

In summary, this work is considered as a conceptual point of departure for the description of localization based on the concept of regularized strong discontinuities in the geometrically nonlinear regime. Clearly, possible extensions are on the one hand the direct inclusion of the discontinuity within

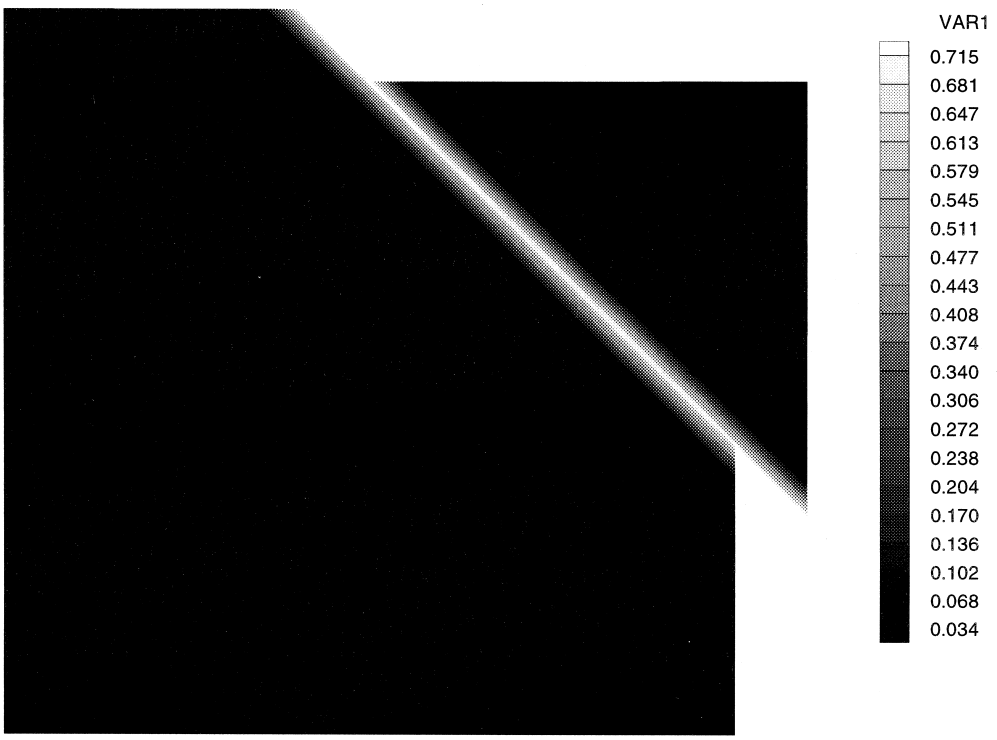


Fig. 16. Deformed configuration and plastic zone $10 \times 10$ $P2$ and $I2$ discretization.

the domain of a finite element and on the other hand the selection of interface constitutive laws which are independent from the constitutive description in the continuous solution domains. Moreover, the proposed formulation could conceptually be extended within a regularized continuum description in order to capture the ultimate, i.e. the discontinuous stage of a failure process.

## References

Armero, F., Garikipati, K., 1996. An analysis of strong discontinuities in multiplicative finite strain plasticity and their relation with the numerical simulation of strain localization in solids. Int. J. Solids Structures 33, 2863–2886.

Gens, A., Carol, I., Alonso, E.E., 1988. An interface element formulation for the analysis of soil–reinforcement interaction. Comp. Geotech. 7, 133–151.

Larsson, R., 1995. A general fictitious crack model based on plastic localization and discontinuous approximation. Int. J. Num. Meth. Engr. 38, 3167–3188.

Larsson, R., Runesson, K., 1996. Element-embedded localization band based on regularized strong discontinuity. J. Engr. Mech., ASCE 122, 402–411.

Larsson, R., Runesson, K., Ottosen, N.S., 1993. Discontinuous displacement approximation for capturing plastic localization. Int. J. Num. Meth. Engr. 36, 2087–2105.

Larsson, R., Runesson, K., Sture, S., 1996. Embedded localization band in undrained soil based on regularized strong discontinuity — theory and FE-analysis. Int. J. Solid Structures 33, 3081–3101.

Miehe, C., Schröder, J., 1994. Post-critical discontinuous localization analysis of small-strain softening elastoplastic solids. Arch. Appl. Mech. 64, 267–286.

Oliver, J., 1996. Modelling strong discontinuities in solid mechanics via strain softening constitutive equations. Part 1: Fundamental and Part 2: Numerical simulation. Int. J. Num. Meth. Engr. 39, 3575–3623.

Simo, J.C., Oliver, J., Armero, F., 1993. An analysis of strong discontinuities induced by strain-softening in rate-independent inelastic solids. Comp. Mech. 12, 277–296.

Schellekens, J.C.J., de Borst, R., 1993. On the numerical integration of interface elements. Int. J. Num. Meth. Engr. 36, 43–66.

Steinmann, P., 1999. A finite element formulation for strong discontinuities in fluid saturated porous media, Int. J. Mech. Cohesive–Frictional Mat. 4, 133–152.

Steinmann, P., Willam, K., 1994. Finite element analysis of elastoplastic discontinuities. J. Engr. Mech., ASCE 120, 2428–2442.

Steinmann, P., Larsson, R., Runesson, K., 1997. On the localization properties of multiplicative hyperelasto-plastic continua with strong discontinuities. Int. J. Solids Structures 34, 969–990.